

Frequency-Modulated Combs via Field-Enhancing Tapered Waveguides

Urban Senica,* Alexander Dikopoltsev, Andres Forrer, Sara Cibella, Guido Torrioli, Mattias Beck, Jérôme Faist, and Giacomo Scalari*

Frequency-modulated (FM) combs feature flat intensity spectra with a linear frequency chirp, useful for metrology and sensing applications. Generating FM combs in semiconductor lasers generally requires a fast saturable gain, usually limited by the intrinsic gain medium properties. Here, it is shown how a spatial modulation of the laser gain medium can enhance the gain saturation dynamics and nonlinearities to generate self-starting FM combs. This is demonstrated with tapered planarized terahertz (THz) quantum cascade lasers (QCLs). While simple ridge THz QCLs typically generate combs presenting a mixture of amplitude and frequency modulation, the on-chip field enhancement resulting from extreme spatial confinement leads to an ultrafast saturable gain regime, generating a pure FM comb with a flatter intensity spectrum and a clear linear frequency chirp. The observed linear frequency chirp is reproduced using a spatially inhomogeneous mean-field theory model, which confirms the crucial role of field enhancement. In addition, the modified spatial temperature distribution within the waveguide results in an improved high-temperature comb operation, up to a heat sink temperature of 115 K, with comb bandwidths of 600 GHz at 90 K. The spatial inhomogeneity leads as well to very intense radio frequency (RF) beatnotes up to -30 dBm and facilitates dynamic switching between various harmonic states in the same device.

heterostructure.^[1] Owing to their relatively fast gain saturation nonlinear properties, they can operate as frequency combs^[2,3] and dual combs.^[4] Along with their significantly higher output powers than THz time-domain spectroscopy systems^[5] for frequencies above ≈ 1.5 THz, these devices are appealing for use in broadband coherent spectroscopy and sensing.

Recent important milestones in THz QCL development include advances in high-temperature narrowband operation,^[6–8] comb formation in ring cavities,^[9] spontaneous pulses from solitons,^[10] heterogeneous integration on silicon substrates,^[11] operation as fast detectors,^[12,13] and the development of a planarized waveguide platform with improved dispersion, radio frequency (RF) and thermal properties.^[14]

For use in spectroscopy, combs with flat intensity spectra are often desired, as this relaxes the conditions on the required signal-to-noise ratio (or integration time) for measuring all the spectral components. From this perspective,

mid-infrared (mid-IR) QCLs are considered more suitable than THz QCLs due to their fast saturable gain, which is the main cause of self-starting frequency-modulated (FM) combs.^[15] Besides producing a flat intensity spectrum, their linear frequency chirp and parabolic phase profile also make external pulse compression schemes relatively straightforward.^[16]


In THz QCLs, the longer upper state lifetimes produce free-running comb states which are a mixture of amplitude and frequency modulation.^[2] The amplitudes of the individual lines in the comb spectrum can often vary significantly, and comb operation is also limited to relatively low operating temperatures.

In this work, we show that spatial variation along the cavity, specifically tapering the laser ridge, can lead to an effective increase in the speed of gain saturation dynamics. We find that the spatial field enhancement leads to an ultrafast saturable gain regime that produces pure FM combs with a flatter intensity spectrum and a linear frequency chirp. Moreover, the spatial modulation of the cavity width results in strong measured RF beatnotes, improves the resilience to high temperatures and also enables switching between various harmonic comb states on a single device.

1. Introduction

Terahertz (THz) quantum cascade lasers (QCLs) are compact sources of coherent THz radiation based on intersubband transitions in an engineered semiconductor superlattice

U. Senica, A. Dikopoltsev, A. Forrer, M. Beck, J. Faist, G. Scalari
Quantum Optoelectronics Group
Institute for Quantum Electronics, ETH Zürich
Zürich 8093, Switzerland
E-mail: usenica@phys.ethz.ch; scalari@phys.ethz.ch
S. Cibella, G. Torrioli
Istituto di Fotonica e Nanotecnologie
CNR
Via del Fosso del Cavaliere 100, Rome 00133, Italy

 The ORCID identification number(s) for the author(s) of this article can be found under <https://doi.org/10.1002/lpor.202300472>

© 2023 The Authors. Laser & Photonics Reviews published by Wiley-VCH GmbH. This is an open access article under the terms of the Creative Commons Attribution License, which permits use, distribution and reproduction in any medium, provided the original work is properly cited.

DOI: 10.1002/lpor.202300472

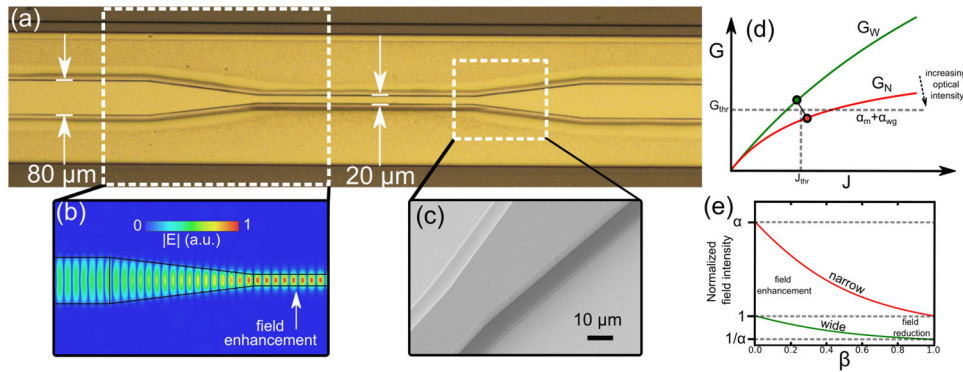


Figure 1. a) Optical microscope image of a tapered device, where wide (80 μm) and narrow (20 μm) sections are connected via adiabatic linear tapers. b) The E-field distribution obtained from full-wave 3D numerical simulations reveals a strong field enhancement effect in the narrow taper sections. Assuming no scattering loss or overlap factor reduction, the field intensity enhancement is proportional to the width ratios, in this case 4:1. This results in an enhanced four-wave mixing nonlinear process, crucial for frequency comb generation. c) Scanning electron microscope (SEM) image of the tapered active waveguide after the dry etching process step with visible vertical, smooth sidewalls. Subsequently, the active waveguides are planarized with a low-loss polymer Benzocyclobutene (BCB) and covered with an extended top metallization. d) Illustration of the gain in the wide and narrow sections, including intensity-dependent gain saturation. In the narrow sections, due to stronger gain saturation and photon-driven transport, the gain is lower but more nonlinear. e) Field intensity in the narrow and wide sections as a function of the width ratios α and the fraction of the device length with narrow sections β . The values are normalized to the field intensity of a homogeneous waveguide with the same properties and operation point.

2. Results and Discussion

2.1. Tapered Planarized Waveguide Geometry

We designed and fabricated tapered waveguides using a homogeneous broadband THz QCL active region^[17] and our planarized waveguide platform.^[14] As shown in the optical microscope image in Figure 1a, the tapered waveguide consists of a sequence of wide (80 μm) and narrow (20 μm) sections connected with adiabatic linear tapers that minimize scattering losses. While in the mid-IR, tapered active waveguide geometries have recently been shown to improve the frequency comb performance due to a lower overall chromatic dispersion,^[18] in our implementation there are several other crucial effects due to the tapered geometry.

The narrow sections act as a filter for selecting the fundamental transverse waveguide mode (required for comb operation with regular teeth),^[19] without using any side absorbers. The wider sections provide more gain for higher output power and a broader emission spectrum due to lower waveguide losses. While fabricating a homogeneous waveguide with the narrow width of 20 μm would be beneficial for transversal mode selection and heat dissipation, the increased dispersion and waveguide losses would severely limit the total comb bandwidth and output power. The propagating mode simulations in Figure 1b show the efficient, scattering-free transition between the wide and narrow sections, which do not affect the formation of longitudinal modes and standing waves along the cavity length.

2.2. Field Enhancement and Nonlinearity

Due to the non-homogeneous waveguide width, there is a field enhancement effect in the narrow sections, as shown in the simulation results in Figure 1b. Considering an idealized case (neglecting any reflection or scattering loss and reduction of the overlap factor Γ), the field intensity enhancement (FIE) is proportional to the width ratio between the wide and narrow sec-

tions (in this case 4:1), while the field amplitude enhancement (FAE) scales with the square root of the ratio ($\sqrt{4}:1 = 2:1$). This is an important aspect, as the spontaneous frequency comb formation in QCLs is based on the nonlinear four-wave mixing process.^[20] Since the latter is a third-order process, its efficiency is proportional to the cube of the electric field intensity.^[21] For example, if we consider the case of non-degenerate four-wave mixing with two initial frequencies of ω_1 and ω_2 , due to the $\chi^{(3)}$ (Kerr) nonlinearity within the active region waveguide,^[22] two new frequencies $\omega_3 = 2\omega_1 - \omega_2$ and $\omega_4 = 2\omega_2 - \omega_1$ will be generated with an output field intensity proportional to $I_3 \propto |\chi^{(3)}|^2 I_1^2 I_2$ and $I_4 \propto |\chi^{(3)}|^2 I_1 I_2^2$, where I_i is the field intensity of the lasing mode at frequency ω_i .^[23]

The nonlinearity within the active region arises mainly from gain saturation, i.e., the fact that the gain changes as a function of the intracavity optical field intensity:^[24]

$$g = \frac{g_0}{1 + I/I_{\text{sat}}} \quad (1)$$

where g_0 is the unsaturated gain, I the intracavity optical field intensity, and I_{sat} the saturation intensity.

With an increasing intracavity optical intensity, the gain will be reduced, while the nonlinearity will be enhanced (and vice versa). Since the active region of a QCL is providing both gain and nonlinearity, a trade-off between these two quantities arises naturally in ridge devices with a constant width. Achieving a good figure of merit in both simultaneously is challenging, as the nonlinearity will be maximum in the highly saturated gain response. With the tapered waveguide, we can, however, use the best of both: the wide sections provide a larger gain, while the narrow sections provide an increased nonlinearity, which is a regime generally not accessible without field enhancement.

This is illustrated in Figure 1c, where we plot the modal gain at an increasing current density through the active region. The dependence for the wide (G_W) and narrow (G_N) sections were com-

puted using the relation from Equation (1) with $I_N = 4 \times I_W$, and with the assumption that the unsaturated gain g_0 is increasing linearly with the applied laser bias.^[25] Due to the field enhancement effect, the gain in the narrow sections is decreased while the nonlinearity increases (larger curvature). To sustain lasing, the total gain of the cavity must overcome the total cavity losses (waveguide + mirror losses, as indicated by the gray horizontal line). The operating point is marked with the colored circles: due to the reduced gain in the narrow sections, the wider sections operate at a point with a higher gain.

While the relative field intensities in the narrow sections are enhanced by the width ratio compared to the wider sections, it is the absolute field intensities that are crucial in nonlinear processes. For a homogeneous ridge active waveguide, the steady state (average) intracavity field intensity will increase with the length of the cavity and with the mirror reflectivities.

We now compare the intracavity field intensities within a tapered and a ridge waveguide with several simplifying assumptions: both waveguides are made of the same active material, and have the same waveguide losses, mirror reflectivities, and cavity length. The tapered waveguide is approximated as consisting of only the wide and narrow sections, neglecting the tapered transitions between them. Under these assumptions, the threshold gain g_{thr} of both devices would be the same, and we can write:

$$g_{thr} = \underbrace{\frac{(1-\beta)g_0}{1+I_W/I_{sat}}}_{\text{wide sections}} + \underbrace{\frac{\beta g_0}{1+\alpha I_W/I_{sat}}}_{\text{narrow sections}} = \underbrace{\frac{g_0}{1+I_H/I_{sat}}}_{\text{homogeneous waveguide}} \quad (2)$$

here, α is the width ratio between the two sections, and β is the fraction of the narrow sections within the whole device length.

Following from Equation (2), in Figure 1e we show a general plot of the intracavity field intensities within an active multi-section waveguide with saturable gain, consisting of two different widths. The intensities are normalized to a homogeneous ridge waveguide with the same properties and at the same operating point. Depending on the filling factor β , the normalized field enhancement in the narrow sections (red) varies between 1 and α . In the wide sections (green), the field is reduced to normalized values between 1 down to $1/\alpha$. We should note that the curvature of the dependence as a function of β (and consequently the normalized field enhancement at a specific point) changes also with the operation point (laser bias).

From this, we can draw some more general conclusions for designing tapered waveguides. For maximal field enhancement in the narrow parts, α should be large and β small. For minimizing the field in the wider section, both α and β should be large (a similar approach is used in tapered amplifiers, where the field intensity spreads out in the tapered sections to reduce gain saturation).^[26] However, for nonlinear processes, the interaction length within the waveguide matters as well, so for a given application, the optimal β will lie somewhere between 0 and 1. Moreover, in practical devices also α cannot be arbitrarily large. For example, in our THz QCL geometry, the narrow sections are limited by the increasing waveguide losses and reduction of the mode overlap factor, while the wider sections are limited by a worse thermal figure of merit.

2.3. Measured devices

In the following, we present measurement results of a 4.2 mm long tapered device with a total of three wide (80 μm) and two narrow (20 μm) sections, with cleaved end facets. For this specific device, $\beta = 0.36$, while $\alpha = 3.16$ (extracted from 3D electromagnetic wave propagation simulations). Its performance is also compared to a reference planarized ridge waveguide with a constant width of 40 μm and a length of 2.7 mm, fabricated during the same process run on the same chip. The width of 40 μm has been chosen as close to optimal for broadband comb operation on simple ridge devices.^[14] In particular, a wider width (e.g., 80 μm) would result in multi-transverse mode laser operation (preventing the formation of a regular comb state)^[19] and an excessive device heating, while a narrower width (e.g., 20 μm) would have larger waveguide losses and result in narrower comb bandwidths. Moreover, 40 μm is close to the geometric mean of the tapered waveguide widths. The calculated field intensity in the narrow tapered sections is around 2.8 times higher compared to the reference ridge device. Here, we included both the α and β factors of the tapered device geometry, as well as the ratio of the device lengths (the average steady-state intracavity field intensity is assumed to be approximately proportional to the total length). Both devices were soldered on copper submounts with custom RF-optimized printed circuit boards (PCBs)^[14] and mounted on a flow cryostat.

2.4. Measured THz Spectrum and RF Beatnote

In Figure 2a–c, we show a typical THz spectrum and RF beatnote measurement of the tapered device, which highlights several performance improvements of the tapered geometry. The measurement was done at a relatively high heat sink temperature of 90 K, and the comb spectrum spans around 600 GHz. In contrast to ridge devices, where the individual mode amplitudes typically vary over several orders of magnitude, we observe a flatter comb spectrum, where the modes in the central ≈ 300 GHz of the comb are within a ≈ 10 dB intensity variation. The measured free-running RF beatnote power is nearly -30 dBm, which is almost three orders of magnitude higher than for ridge devices processed on the same chip in ref. [14] (with such a large measurement dynamic range of over 55 dB, additional weak spurious lines can appear, but these most likely originate from noise or pick-up from the RF environment and not from the comb state itself). Such a strong measured beatnote amplitude is due to contributions of the field enhancement effect and a larger total intracavity optical power (larger device area with wider sections).

The dependence of the measured RF beatnote intensity on the field enhancement can easily be explained with the following expression: as the free-running RF beatnote is a direct measurement of the current modulation $\Delta I(t)$ at the mode spacing frequency f_{rep} , its intensity is proportional to the sum of the product of the neighboring modes' complex electric field amplitudes:^[27]

$$\Delta I(t) \propto \sum_i E_i E_{i+1}^* \quad (3)$$

here, E_i, E_{i+1}^* are the electric field amplitudes of two neighboring modes in the THz emission spectrum, which contribute to a

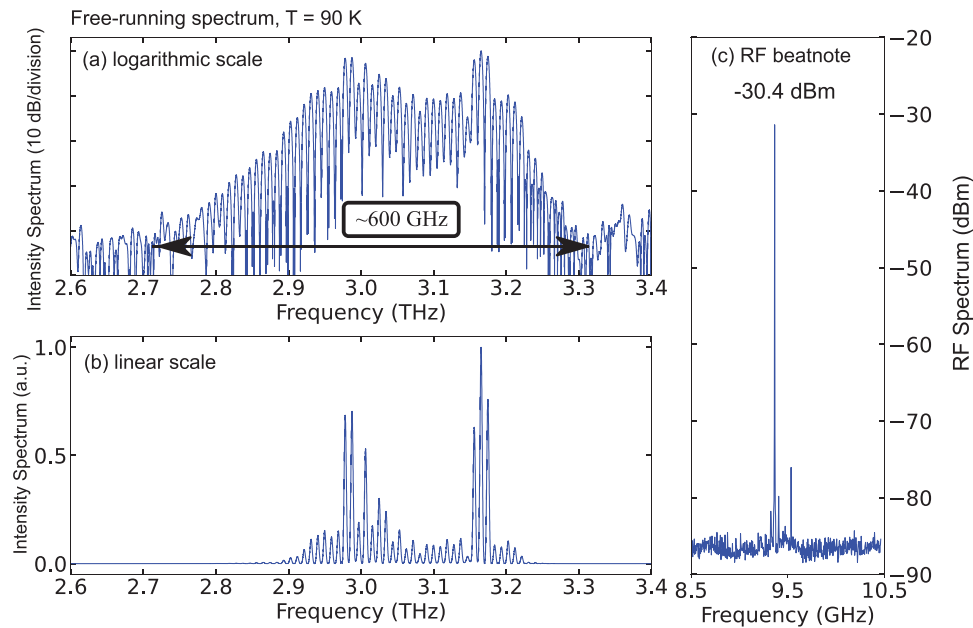


Figure 2. a) Measured THz emission spectrum in logarithmic scale with a comb bandwidth of around 600 GHz at a heat sink temperature of 90 K. b) The same measured spectrum in linear scale displays a relatively flat comb spectrum between 2.9–3.2 THz. c) Measured RF beatnote at the roundtrip frequency, up to nearly -30 dBm.

measurable signal at f_{rep} . Typical measured beatnotes also display narrow linewidths, in the order of ≈ 1 kHz.

For tapered devices at such elevated heat sink temperatures (90 K as opposed to the more standard 15–40 K),^[28,29] the comb bandwidth is reduced due to two main contributions: increased waveguide losses in the narrow sections (20 μm), and the decreased gain due to an increased heat sink temperature. This results in the absence of the low frequency part of the emission spectrum for this epilayer (down to ≈ 2.4 THz).

However, at lower heat sink temperatures (40 K), a comparable comb bandwidth to those obtained with simple planarized ridges with a width of 40 μm is observed (typically spanning 700–800 GHz at 40 K). THz emission and RF beatnote spectra as a function of laser bias are shown in Figures S1 and S2 (Supporting Information), along with a movie of a laser bias sweep, which displays a rich landscape of fundamental and harmonic comb states. Additionally, a comparison of measured comb spectra of the ridge and tapered devices is in Figure S3 (Supporting Information), where it is evident that the tapered devices feature a significantly flatter envelope of the spectrum intensity.

2.5. Linear Chirp and Flatter Spectrum

We then performed Shifted Wave Interference Fourier Transform (SWIFT) spectroscopy measurements^[2,30] to assess the comb coherence and reconstruct the time domain profile using a fast hot electron bolometer (HEB) detector^[31,32] (a more detailed explanation of the working principle and setup used is in ref. [14]). A relatively weak RF signal (-10 dBm at the output of the RF source) was injected at the roundtrip frequency f_{rep} to stabilize the comb repetition rate and to give the QCL and the spectrum analyzer a common time-base allowing the IQ demodulation. For such a

weak RF injection power it is assumed that the comb is stabilized without perturbing its free-running state (namely, the specific intensity spectrum and intermodal phases). In **Figure 3a**, we plot both the spectrum product and the SWIFT spectrum. The first was obtained by measuring the DC interferogram with a slow deuterated triglycine sulfate (DTGS) detector, while the latter was reconstructed with IQ demodulation from optical beatnote measurements with a fast detector (HEB). The excellent agreement and comparable signal-to-noise ratio is an indicator of good comb coherence, while also the detected optical beatnote measured on the HEB is in the order of 20–30 dB stronger than for planarized ridge samples. The reconstructed intermodal phase profile in this state follows a linear chirp, which is typically observed in mid-IR QCLs,^[33,34] but has not yet been reported so clearly in THz QCLs. In THz QCL designs optimized for comb operation, the longer upper state lifetime ($\tau_{\text{up}} > 10$ ps) and consequently the larger $\omega_{\text{rep}} \times \tau_{\text{up}}$ product typically makes the comb state exhibit considerable amplitude modulations in the time-domain output signal. To experimentally confirm the crucial role of field enhancement, we also performed SWIFT spectroscopy on the reference planarized ridge sample. As shown in Figure S4 (Supporting Information), the intermodal phases are flat over a major part of the spectrum, generating a periodic waveform with strong amplitude modulations and an oscillating instantaneous frequency, without a linear chirp. This is in good agreement with the various measurement and simulation results of ridge waveguide THz QCL combs presented in refs. [34–37]. The situation is different in mid-IR QCL combs, where ultrafast gain saturation and gain asymmetry (arising from non-parabolicity and Bloch gain)^[22] play a major role in driving the laser dynamics.

The reconstructed time-domain profile of the tapered device has a quasi-continuous periodic output intensity with some oscillations, and the instantaneous frequency produces a linear chirp,

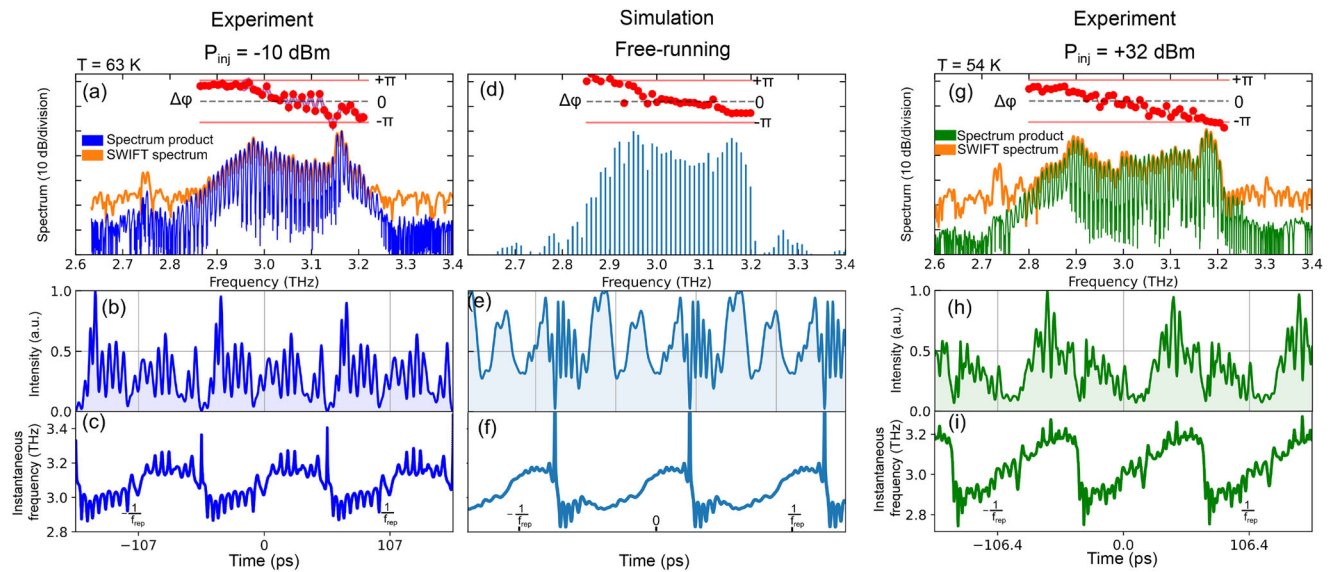


Figure 3. SWIFT spectroscopy measurements and mean-field theory simulations of the tapered waveguide device. a–c) Measurements on a weakly RF-injected (-10 dBm) tapered device produce a relatively flat comb emission spectrum, a linear frequency chirp and a quasi-continuous output intensity with some oscillations. d–f) Results of mean-field theory simulations with a spatial dependence of the crucial parameters are able to reproduce the main features of the measured device. g–i) Measurement results of the same tapered device under strong RF-injection (+32 dBm) with a broadened comb emission spectrum and a cleaner linear frequency chirp with a more constant output intensity on top of a sine wave that follows the RF modulation.

both are shown in Figure 3b, c. This could indicate that the effects related to the field enhancement push the tapered THz QCL comb toward a regime similar to mid-IR QCL combs, with a flatter intensity spectrum and a linear chirp in frequency.

Indeed, another aspect of the field enhancement is the increased photon-driven current^[38] in the narrow sections, which shortens the stimulated carrier lifetime τ_{st} through the dependence:

$$\tau_{st} = \frac{1}{g_c S} \quad (4)$$

where g_c is the gain cross-section and S the photon flux (per period and unit active region width). This results in a reduction of the upper state lifetime $\tau_{up}^{-1} = \tau_{nr}^{-1} + \tau_{sp}^{-1} + \tau_{st}^{-1}$, where τ_{nr} , τ_{sp} are the non-radiative and spontaneous emission lifetimes, respectively. With this effective lifetime shortening, the tapered waveguide system is led into a fast saturable gain regime, where the laser tends to produce a continuous waveform with a quasi-constant optical intensity, manifested as frequency-modulated combs usually observed in mid-IR QCLs.^[15]

Specifically for the measured devices, the spontaneous emission lifetime is in the order of microseconds (and can be neglected), while the non-radiative lifetime is around 20 ps (see Supplementary Material of ref. [39]). The estimated stimulated and upper state lifetimes and the effect of the tapered geometry can be calculated, also considering that the photon flux S follows the same dependence as the field intensity and is therefore an estimated factor of 2.8 times higher in the narrow taper sections compared to the reference ridge device. Detailed calculations with two different approaches can be found in the Supporting Information. Both methods give a very comparable and significantly reduced value of the upper state lifetime with the tapered wave-

guide geometry. In particular, the upper state lifetime τ_{up} in the reference ridge device is estimated at around 9.5 (or 7.5) ps and reduced to 5 (or 3.5) ps in the narrow taper sections (both at maximum bias conditions).

To study the mechanism driving the comb dynamics, we developed a model that includes a spatial dependence of the optical nonlinearities, gain saturation, and temperature distribution within the cavity (by modifying the gain profile), and performed numerical simulations following a mean-field theory approach based on ref. [40]. The details of the model as well as all the simulation parameters used (Table S1, Supporting Information) along with the frequency-dependent waveguide and material dispersion (Figure S6, Supporting Information) can be found in the Supporting Information. Results obtained with our model have good agreement with the experimental results. As shown in Figure 3d–f, the simulation produces a relatively flat spectrum separated into two main lobes with a phase distribution similar to the measured result. The linear frequency chirp is also reproduced in simulation, with a discontinuity at the phase jump point. The time domain profile reconstructs the quasi-continuous intensity with oscillations and individual points in time where the intensity almost vanishes, again consistent with the measurements. From the simulation model, we found that the spatial dependence of the nonlinearities and gain are crucial for obtaining these specific kinds of comb states.

Successively, when increasing the RF injection power up to +32 dBm, the comb spectrum is further broadened and flattened, and the observed linear chirp has a cleaner shape, as visible in Figure 3g–i. The THz intensity spectrum features a flatter profile as well, while its time domain intensity profile is modulated in amplitude, following the strong RF-injected cosine profile ($\propto \cos(2\pi f_{rep} t)$). These observations are similar to the findings of extensive mid-IR QCL simulations reported in ref. [41]. There, due

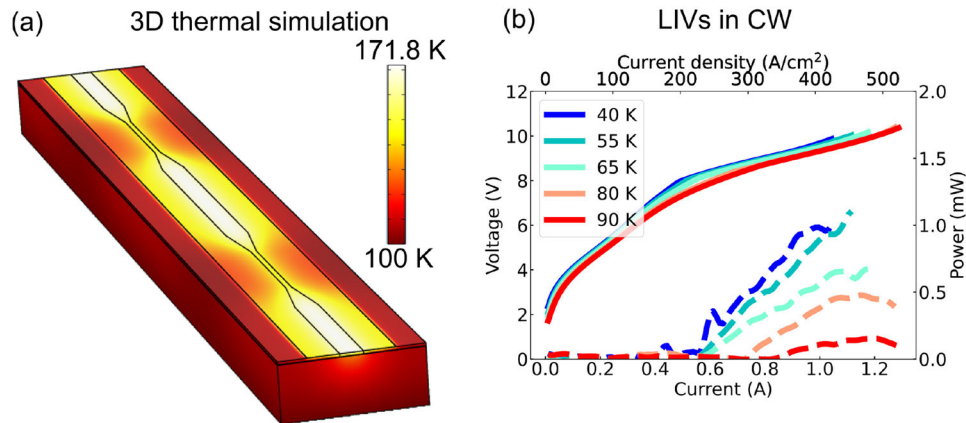


Figure 4. a) 3D thermal COMSOL simulations of the tapered device at the maximum laser bias and a heat sink temperature of 100 K. While the wider sections are heating up more, they are separated into smaller islands where the narrower sections act as heat dissipation channels with a lower operating temperature. b) High-temperature LIV characteristics of a tapered device in CW.

to a non-zero third-order dispersion in the mid-IR QCL cavity, the intensity spectrum features oscillations in amplitude and the intermodal phases form groups, diverging from an ideal linear chirp (which is similar to some states observed in free-running THz QCLs). By means of RF injection, a clean linear chirp and flatter spectral amplitudes can be recovered, which is consistent also with our experimental results with the tapered planarized waveguide geometry.

2.6. High-Temperature Performance

Improved frequency comb properties are maintained for even higher operating temperatures. Results of a 3D COMSOL thermal simulation in **Figure 4a** show that the wider sections, which are heating up more, are separated into smaller islands and the connecting narrower regions act as heat dissipation channels. In

the thermal simulations, typical maximum bias conditions (11 V, 400 A cm^{-2}), a heat sink temperature of 100 K, and the following material heat conductivities were used: $\text{Cu} = 320 \text{ W m}^{-1}\text{K}^{-1}$, $\text{GaAs/AlGaAs active region} = 5 \text{ W m}^{-1}\text{K}^{-1}$,^[42] $\text{GaAs substrate} = 100 \text{ W m}^{-1}\text{K}^{-1}$, $\text{BCB} = 0.15 \text{ W m}^{-1}\text{K}^{-1}$ (half of the reported room temperature conductivity).^[43,44]

In **Figure 4b**, we plot LIV curves measured in continuous wave (CW) operation. The power measurements were performed with a large area Thomas Keating absolute THz power meter and a chopper wheel, with limited sensitivity and without any correction for collection losses, so they could not be performed up to the maximum lasing temperature. Measured with a room-temperature DTGS detector inside a Fourier transform infrared spectrometer (FTIR), the maximum lasing temperature in CW was as high as 118 K.

In **Figure 5a, b**, we compare the high-temperature comb operation of the tapered waveguide and the reference ridge waveguide,

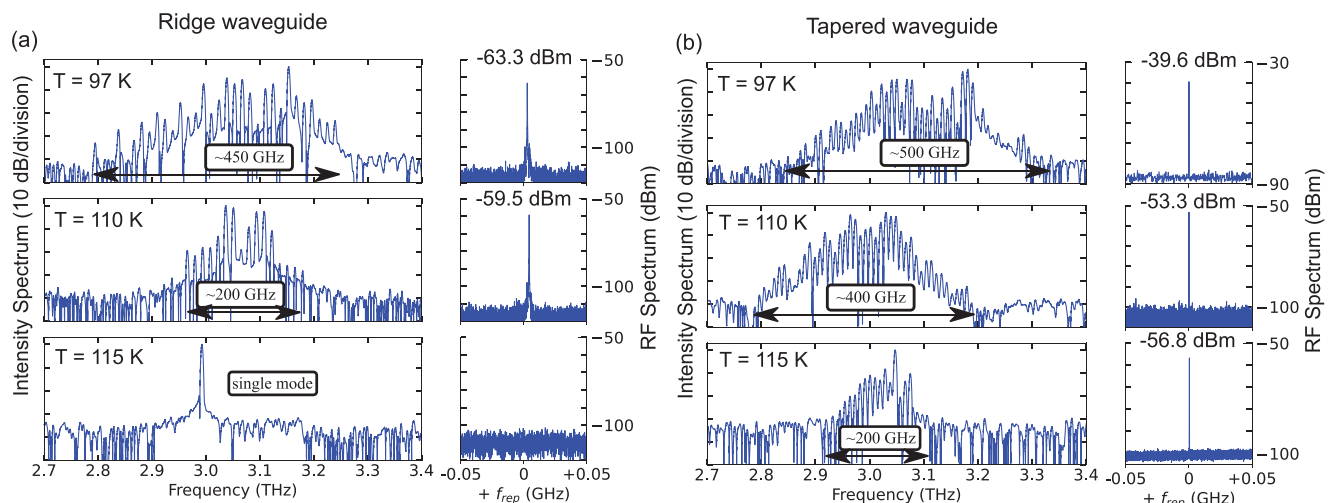


Figure 5. Measured spectra and free-running RF beatnotes at high operating temperatures, comparing a) a ridge waveguide ($W = 40 \mu\text{m}$, $L = 2.7 \text{ mm}$) and b) a tapered waveguide device ($W = 80/20 \mu\text{m}$, $L = 4.2 \text{ mm}$). The tapered waveguide device displays broader THz bandwidths, flatter emission spectra, stronger RF beatnotes, and a higher maximum comb temperature of 115 K. The spectra were obtained with a room-temperature DTGS detector.

which has a maximum lasing temperature in CW up to 116.5 K. Comparing the two samples at the same heat sink temperatures, it can be observed that the tapered waveguide device features a broader comb bandwidth and a stronger RF beatnote. Comb operation is maintained up to 115 K, still with a bandwidth of ≈ 200 GHz with a strong single RF beatnote above -60 dBm. This improved high-temperature comb performance is attributed to two main contributions. The first is the field enhancement effect giving rise to stronger nonlinearities and gain saturation which affect the comb formation process. Second, the narrow sections are at a significantly lower temperature than the wider regions (simulation results indicate a difference of ≈ 25 degrees).

A more detailed thermal simulation result analysis can be found in Figure S5 (Supporting Information), where the line cuts across different profiles of the device show a complex temperature distribution due to the non-homogeneous geometry consisting of materials with different thermal properties.

We should also note here that the observed threshold current density of around 180 Acm^{-2} at 40 K in CW of this device is higher than the ones we reported for simple planarized ridges with a width of $40 \mu\text{m}$ (140 Acm^{-2} at 40 K), which is due to increased waveguide losses and gain saturation in the narrow sections with a width of only $20 \mu\text{m}$.

2.7. Harmonic Comb State Switching

Another unique feature of the tapered geometry is the possibility to switch to various harmonic comb states on demand. Recently, such harmonic comb states, where the lasing mode spacing is an integer of the fundamental f_{rep} , have gained interest in the QCL community.^[45] In mid-IR QCLs, engineered defects have been fabricated for selecting a specific harmonic order,^[46] while in THz these have been so far limited to spontaneously forming harmonic states without an external control.^[39,47] As our tapered devices have a non-uniform shape along the length of the device, they are prone to switch to harmonic comb states. We demonstrate harmonic comb state switching, where a number of pure harmonic comb states can be excited simply by varying the bias and temperature on a single tapered waveguide device. If we look at a fundamental comb state in Figure 6a, b, we can measure a strong RF beatnote at the fundamental f_{rep} , but also at higher harmonics up to the 7th harmonic (limited by the spectrum analyzer bandwidth of 67 GHz). This is an indication of strong comb coherence (maintained also between more distant comb lines). By varying the laser bias and temperature, we can switch between the fundamental and the 2nd, 3rd, 4th, and 6th harmonic states, as shown in Figure 6b–f, respectively. These are pure harmonic comb states, as we detect a single RF beatnote only at the frequency of the harmonic mode spacing, without any other signals present in the RF spectrum.

An interesting aspect is that the THz emission bandwidth of harmonic comb states is typically larger than for fundamental comb states, covering ≈ 700 GHz for the 6th harmonic in Figure 6f even at elevated heat sink temperatures above 80 K. In contrast to fundamental states, where multi-beatnote or incoherent states are also observed, harmonic states appear almost exclusively in a pure comb state. The harmonic combs in tapered devices produce strong RF beatnotes also for very high RF frequencies, still

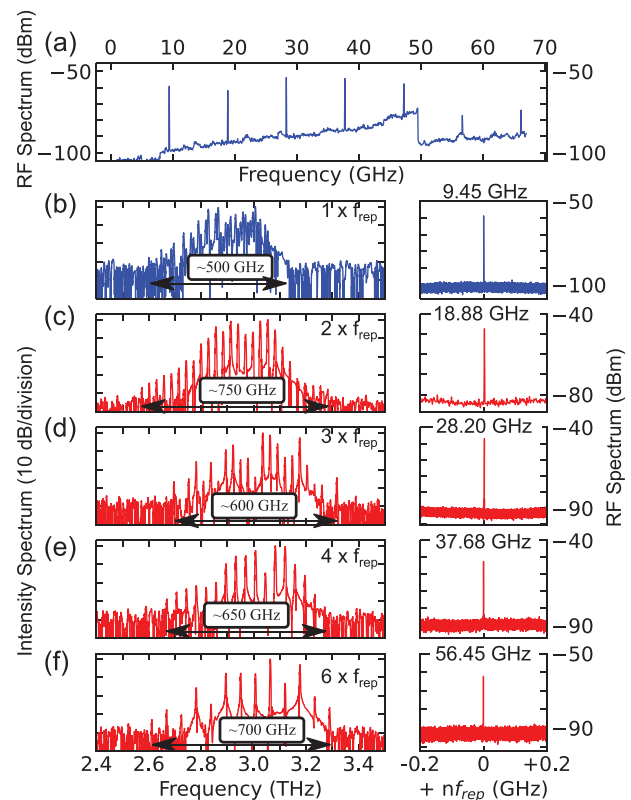


Figure 6. Harmonic comb state switching: on a single tapered device, various pure harmonic comb states can be excited by varying the laser bias and temperature. a) RF spectrum measured on a fundamental comb state from panel (b) shows strong RF signals at the fundamental and multiples of the repetition rate f_{rep} , up to the 7th harmonic (limited by the spectrum analyzer range). b–f) highlights the measured spectra and RF beatnotes of the pure fundamental (blue) and harmonic comb states (red). All of the measurements were performed at a heat sink temperature of 80 K or higher, and there are no other RF signals present besides the strong single beatnote.

with a measured intensity of nearly -60 dBm at 56 GHz (we should note that this is without any correction for increased high-frequency cable and PCB losses). This feature makes them appealing also as reliable coherent sources of high-frequency RF signals or even millimeter waves.^[45,48]

In the Supporting Information, we added some more simulation details, including an analysis of 3D simulation results of the RF-field distribution at the corresponding harmonic microwave resonances (Figures S7 and S8, Supporting Information), along with some additional explanation as to why the 5th and 7th harmonic comb states were not observed experimentally on this specific tapered device.

3. Conclusion

In conclusion, we have presented a method to engineer the comb states in THz QCLs by spatially modulating the transverse dimension of a Fabry-Pérot resonator. Such geometries are enabled by the planarized waveguide platform. A strong field enhancement effect results in an enhanced four-wave mixing process and gain saturation, both crucial for comb formation in THz QCLs.

Measured devices produce flatter comb spectra spanning 600 GHz at a heatsink temperature of 90 K, with strong RF beatnotes up to nearly -30 dBm. Improved comb properties are maintained for high operating temperatures, with a comb bandwidth of 200 GHz at 115 K. We also report on the first experimental observation of a clear linear frequency chirp in a THz QCL, due to the device operating in a fast saturable gain regime. We are able to reproduce the results with a mean-field theory simulation model with a spatial dependence of the optical nonlinearities, gain saturation, and active region temperature.

In a broader context, electromagnetic environment engineering strongly affects light-matter interaction. One may consider our experiments as an analog to the Purcell effect, where spontaneous emission can be enhanced by light confinement in a cavity.^[49] In our work, the presence of strong subwavelength confinement with field enhancement leads to an ultrafast stimulated emission lifetime affecting the laser dynamics.

It is important to emphasize that the presented field enhancement approach is not limited to THz QCLs, but can be applied to a variety of other laser systems,^[50] where a modified photon flux can be used to change the upper state lifetime and affect the laser dynamics through the $\omega_{\text{rep}} \times \tau_{\text{up}}$ product. For example, in spectroscopy, a flatter comb spectrum is desired, and this can be produced with FM combs via strong field enhancement, as demonstrated in this work ($\omega_{\text{rep}} \times \tau_{\text{up}}$ is small). On the other hand, an increased waveguide cross-section would reduce gain saturation leading to slower dynamics, possibly facilitating short pulse formation in the presence of an increased $\omega_{\text{rep}} \times \tau_{\text{up}}$ product. For the specific devices presented in this work, the $\omega_{\text{rep}} \times \tau_{\text{up}}$ products are 0.79, 0.60, and 0.25 for the homogeneous ridge and for the wide and the narrow taper sections, respectively (the mean value of the computed lifetimes with two different approaches was used).

The tapered geometry also enables the switching between various pure harmonic comb states with increased comb bandwidths up to 750 GHz above 80 K. With the planarized waveguide platform, it should also be possible to engineer the switching to harmonic comb states by, for example, designing only the extended top metallization to match the shape of the harmonic RF field (by following the position of nodes and antinodes), without increasing waveguide losses, as is the case in the tapered active waveguide geometry. This should in turn lead to increased absolute harmonic comb bandwidths.

Beyond improved frequency comb performance, such integrated field enhancement structures can be used to boost the nonlinear optical properties originating from the large $\chi^{(2)}$ and $\chi^{(3)}$ nonlinearities within the active region, which could lead to novel effects and functionalities, such as the generation of new frequencies (e.g., via difference frequency^[51] and/or harmonic generation).^[52]

Supporting Information

Supporting Information is available from the Wiley Online Library or from the author.

Acknowledgements

The authors gratefully acknowledged funding from the ERC Grant CHIC (No. 724344) and in part by the Innosuisse (grant 53098.1 IP-ENG), the SNF MINT Project No212735 and Actphast 4 Researchers P2020-41.

Open access funding provided by Eidgenössische Technische Hochschule Zurich.

Conflict of Interest

The authors declare no conflict of interest.

Author Contributions

U.S. and G.S. conceived the idea. U.S. designed and fabricated the devices, carried out all the measurements, analyzed experimental data, and performed electromagnetic and thermal numerical simulations under the supervision of G.S. and J.F. A.D. developed and implemented the spatially inhomogeneous mean-field theory model. A. F. built the SWIFTS setup. S.C. and G.T. provided the HEB detectors. A.F. and G.S. optimized the HEB RF coupling. M.B. performed the epitaxial growth. U.S. and G.S. wrote the manuscript. All authors discussed the results and commented on the manuscript.

Data Availability Statement

The data that support the findings of this study are available from the corresponding author upon reasonable request.

Keywords

field enhancement, frequency combs, frequency modulation, quantum cascade lasers, terahertz

Received: May 24, 2023
Revised: September 4, 2023
Published online: October 30, 2023

- [1] R. Köhler, A. Tredicucci, F. Beltram, H. E. Beere, E. H. Linfield, A. G. Davies, D. A. Ritchie, R. C. Iotti, F. Rossi, *Nature* **2002**, 417, 156.
- [2] D. Burghoff, T.-Y. Kao, N. Han, C. W. I. Chan, X. Cai, Y. Yang, D. J. Hayton, J.-R. Gao, J. L. Reno, Q. Hu, *Nat. Photonics* **2014**, 8, 462.
- [3] M. Rösch, G. Scalari, M. Beck, J. Faist, *Nat. Photonics* **2015**, 9, 42.
- [4] M. Rösch, G. Scalari, G. Villares, L. Bosco, M. Beck, J. Faist, *Appl. Phys. Lett.* **2016**, 108, 171104.
- [5] J. Neu, C. A. Schmuttenmaer, *J. Appl. Phys.* **2018**, 124, 231101.
- [6] L. Bosco, M. Franckić, G. Scalari, M. Beck, A. Wacker, J. Faist, *Appl. Phys. Lett.* **2019**, 115, 010601.
- [7] A. Khalatpour, A. K. Paulsen, C. Deimert, Z. R. Wasilewski, Q. Hu, *Nat. Photonics* **2020**, 15, 16.
- [8] A. Khalatpour, M. C. Tam, S. J. Addamane, J. Reno, Z. Wasilewski, Q. Hu, *Appl. Phys. Lett.* **2023**, 122, 161101.
- [9] M. Jaidl, N. Opačak, M. A. Kainz, S. Schönhuber, D. Theiner, B. Limbacher, M. Beiser, M. Giparakis, A. M. Andrews, G. Strasser, B. Schwarz, J. Darmo, K. Unterrainer, *Optica* **2021**, 8, 780.
- [10] P. Micheletti, U. Senica, A. Forrer, S. Cibella, G. Torrioli, M. Franckić, M. Beck, J. Faist, G. Scalari, *Sci. Adv.* **2023**, 9, eadf9426.
- [11] M. Jaidl, N. Opačak, M. A. Kainz, D. Theiner, B. Limbacher, M. Beiser, M. Giparakis, A. Andrews, G. Strasser, B. Schwarz, J. Darmo, K. Unterrainer, *Appl. Phys. Lett.* **2022**, 120, 091106.
- [12] P. Micheletti, J. Faist, T. Olariu, U. Senica, M. Beck, G. Scalari, *APL Photonics* **2021**, 6, 106102.
- [13] V. Pistore, E. A. A. Pogna, L. Viti, L. Li, A. G. Davies, E. H. Linfield, M. S. Vitiello, *Adv. Sci.* **2022**, 9, 2200410.

- [14] U. Senica, A. Forrer, T. Olariu, P. Micheletti, S. Cibella, G. Torrioli, M. Beck, J. Faist, G. Scalari, *Light: Sci. Appl.* **2022**, *11*, 347.
- [15] N. Opačak, B. Schwarz, *Phys. Rev. Lett.* **2019**, *123*, 243902.
- [16] P. Täschler, M. Bertrand, B. Schneider, M. Singleton, P. Jouy, F. Kapsalidis, M. Beck, J. Faist, *Nat. Photonics* **2021**, *15*, 919.
- [17] A. Forrer, M. Franckić, D. Stark, T. Olariu, M. Beck, J. Faist, G. Scalari, *ACS Photonics* **2020**, *7*, 784.
- [18] R. Wang, P. Täschler, F. Kapsalidis, M. Shahmohammadi, J. Faist, M. Beck, *Optics Letters* **2020**, *45*, 6462.
- [19] D. Bachmann, M. Rösch, M. J. Süess, M. Beck, K. Unterrainer, J. Darmo, J. Faist, G. Scalari, *Optica* **2016**, *3*, 1087.
- [20] A. Hugi, G. Villares, S. Blaser, H. C. Liu, J. Faist, *Nature* **2012**, *492*, 229.
- [21] P. Friedli, H. Sigg, B. Hinkov, A. Hugi, S. Riedi, M. Beck, J. Faist, *Appl. Phys. Lett.* **2013**, *102*, 222104.
- [22] N. Opačak, S. Dal Cin, J. Hillbrand, B. Schwarz, *Phys. Rev. Lett.* **2021**, *127*, 093902.
- [23] R. W. Boyd, *Nonlinear optics*, 3rd ed edition, Academic Press, Amsterdam, Boston **2008**.
- [24] D. Indjin, P. Harrison, R. Kelsall, Z. Ikončić, *J. Appl. Phys.* **2002**, *91*, 9019.
- [25] S. Barbieri, C. Sirtori, H. Page, M. Beck, J. Faist, J. Nagle, *IEEE J. Quantum Electron.* **2000**, *36*, 736.
- [26] J. Walpole, *Opt. Quantum Electron.* **1996**, *28*, 623.
- [27] H. Li, P. Laffaille, D. Gacemi, M. Apfel, C. Sirtori, J. Leonardon, G. Santarelli, M. Rösch, G. Scalari, M. Beck, J. Faist, W. Hänsel, R. Holzwarth, S. Barbieri, *Opt. Express* **2015**, *23*, 33270.
- [28] F. P. Mezzapesa, K. Garrasi, J. Schmidt, L. Salemi, V. Pistore, L. Li, A. G. Davies, E. H. Linfield, M. Riesch, C. Jiruschek, T. Carey, F. Torrisi, A. C. Ferrari, M. S. Vitiello, *ACS photonics* **2020**, *7*, 3489.
- [29] Y. Yang, D. Burghoff, D. J. Hayton, J.-R. Gao, J. L. Reno, Q. Hu, *Optica* **2016**, *3*, 499.
- [30] D. Burghoff, D. Ren, Z. Han, *Opt. Express* **2020**, *28*, 6002.
- [31] A. D. Semenov, G. N. Gol'tsman, R. Sobolewski, *Supercond. Sci. Technol.* **2002**, *15*, R1.
- [32] G. Torrioli, A. Forrer, M. Beck, P. Carelli, F. Chiarello, J. Faist, A. Gaggero, E. Giovine, F. Martini, U. Senica, R. Leoni, G. Scalari, S. Cibella, *Opt. Express* **2023**, *31*, 15942.
- [33] M. Singleton, P. Jouy, M. Beck, J. Faist, *Optica* **2018**, *5*, 948.
- [34] F. Cappelli, L. Consolino, G. Campo, I. Galli, D. Mazzotti, A. Campa, M. Siciliani de Cumis, P. Cancio Pastor, R. Eramo, M. Rösch, M. Beck, G. Scalari, J. Faist, P. De Natale, S. Bartalini, *Nat. Photonics* **2019**, *13*, 562.
- [35] D. Burghoff, Y. Yang, D. J. Hayton, J.-R. Gao, J. L. Reno, Q. Hu, *Opt. Express* **2015**, *23*, 1190.
- [36] S. Markmann, D. Stark, M. Singleton, M. Beck, J. Faist, G. Scalari, *Phys. Rev. Appl.* **2023**, *19*, 064063.
- [37] C. Silvestri, X. Qi, T. Taimre, A. D. Rakić, *Phys. Rev. A* **2022**, *106*, 053526.
- [38] H. Choi, L. Diehl, Z.-K. Wu, M. Giovannini, J. Faist, F. Capasso, T. B. Norris, *Phys. Rev. Lett.* **2008**, *100*, 167401.
- [39] A. Forrer, Y. Wang, M. Beck, A. Belyanin, J. Faist, G. Scalari, *Appl. Phys. Lett.* **2021**, *118*, 131112.
- [40] D. Burghoff, *Optica* **2020**, *7*, 1781.
- [41] N. Opačak, *The origin of frequency combs in free-running quantum cascade lasers*, Ph.D. thesis, Wien, **2022**.
- [42] G. Scamarcio, M. S. Vitiello, V. Spagnolo, S. Kumar, B. Williams, Q. Hu, *Phys. E* **2008**, *40*, 1780.
- [43] C. L. Choy, *Polymer* **1977**, *18*, 984.
- [44] D. Greig, *Cryogenics* **1988**, *28*, 243.
- [45] D. Kazakov, M. Piccardo, Y. Wang, P. Chevalier, T. S. Mansuripur, F. Xie, C.-e. Zah, K. Lascola, A. Belyanin, F. Capasso, *Nat. Photonics* **2017**, *11*, 789.
- [46] D. Kazakov, N. Opačak, M. Beiser, A. Belyanin, B. Schwarz, F. Capasso, M. Piccardo, F. Capasso, *Optica* **2021**, *8*, 1277.
- [47] Y. Wang, A. Belyanin, *Phys. Rev. A* **2020**, *102*, 013519.
- [48] V. Pistore, H. Nong, P.-B. Vigneron, K. Garrasi, S. Houver, L. Li, A. Giles Davies, E. H. Linfield, J. Tignon, J. Mangeney, R. Colombelli, M. S. Vitiello, S. S. Dhillon, *Nat. Commun.* **2021**, *12*, 1427.
- [49] Q. Gu, B. Slutsky, F. Vallini, J. S. Smalley, M. P. Nezhad, N. C. Frateschi, Y. Fainman, *Opt. Express* **2013**, *21*, 15603.
- [50] J. Hillbrand, D. Auth, M. Piccardo, N. Opačak, E. Gornik, G. Strasser, F. Capasso, S. Breuer, B. Schwarz, *Phys. Rev. Lett.* **2020**, *124*, 023901.
- [51] M. A. Belkin, F. Capasso, A. Belyanin, D. L. Sivco, A. Y. Cho, D. C. Oakley, C. J. Vineis, G. W. Turner, *Nat. Photonics* **2007**, *1*, 288.
- [52] C. Gmachl, A. Belyanin, D. L. Sivco, M. L. Peabody, N. Owschimikow, A. M. Sergent, F. Capasso, A. Y. Cho, *IEEE J. Quantum Electron.* **2003**, *39*, 1345.